Preprint: To be

Spectral Irradiance Calibration in the Infrared XI: Comparison of α Boo and 1 Ceres with a Laboratory Standard

Fred C. Witteborn[1]

Space Science Division, Mail stop 245-6, NASA-Ames Research Center, Moffett Field, California 94035

Electronic Mail: witteborn@aol.com

Martin Cohen

Radio Astronomy Laboratory, 601 Campbell Hall, University of California, Berkeley, California 94720

Electronic Mail: mcohen@astro.berkeley.edu

Jesse D. Bregman and Diane Wooden

Space Science Division, Mail stop 245-6, NASA-Ames Research Center, Moffett Field, California 94035

Electronic Mail: bregman@ssa1.arc.nasa.gov,wooden@ssa1.arc.nasa.gov

Karen Heere

Sterling Software, Mail stop 210-9, NASA-Ames Research Center, Moffett Field, California 94035

Electronic Mail:heere@osprey.arc.nasa.gov

Eric L. Shirley

NIST, Optical Technology Division, Bldg. 221, Rm. B-208, Gaithersburg, MD 20899

Electronic Mail: eric.shirley@nist.gov

Received _____; accepted _____

[1] SETI Institute

ABSTRACT

Infrared spectra of two celestial objects frequently used as flux standards are calibrated against an absolute laboratory flux standard at a spectral resolving power of 100 to 200. The spectrum of the K1.5III star, α Boo, is measured from 3 μm to 30 μm and that of the C-type asteroid, 1 Ceres, from 5 μm to 30 μm. While these "standard" spectra do not have the apparent precision of those based on calculated models, they do not require the assumptions involved in theoretical models of stars and asteroids. Specifically they provide a model-independent means of calibrating celestial flux in the spectral range from 12 μm to 30 μm where accurate absolute photometry is not available. The agreement found between the spectral shapes of α Boo and Ceres based on laboratory standards, and those based on observed ratios to α CMa (Sirius) and α Lyr (Vega), flux calibrated by theoretical modeling of these hot stars, strengthens our confidence in the applicability of the stellar models as primary irradiance standards.

Subject headings: infrared — absolute calibration — stars: α Boo — asteroids: 1 Ceres

1. Introduction

This series of papers on spectral irradiance calibration was motivated by the need to establish accurate celestial flux standards for use in astronomical spectroscopy by space-borne, airborne and ground-based instruments. The earlier papers in the series, summarized by Cohen et al. (1996: hereafter referred to as Paper VII), use theoretical models of the A-type stars Vega and Sirius as the fundamental reference standards for spectral shape. The absolute flux levels are determined by independent absolute photometric measurements but these are confined to wavelengths of 11.7 μm and lower. Absolute photometry at longer wavelengths is not sufficiently accurate to test the validity of assumptions in the model stellar atmospheric spectra at wavelengths beyond 12 μm. The purpose of this paper is to show how a laboratory standard. that is well-understood from 3 μm to 30 μm, can be used to calibrate the spectral shape of a celestial standard throughout this range and thus produce absolute flux standards by normalization to the absolute flux levels at and below 11.7 μm.

In this paper the fundamental reference standard for spectral shape is an internationally accredited blackbody whose temperature uncertainty, stability and uniformity are controlled to $\pm$0.13 K (2σ, r.m.s. average). The flux reaching the spectrometer from this standard is simply a Planck radiation function modified by the diffraction effects of the intervening apertures and optics. Calibration of observatory spectra using laboratory spectra is not straightforward. Here we briefly note some of the precautions. In transferring radiation from the blackbody to the spectrometer, care must be taken to ensure that it follows the same optical path through the spectrometer as that taken by radiation from the celestial objects viewed through the telescope. In this case, the telescope was the Kuiper Airborne Observatory (KAO), which was required in order to observe in spectral regions inaccessible from the ground. Furthermore, the signal-plus-background radiation must be low enough

to stay within the linear range of the detector system. Once the spectrometer is properly illuminated by the laboratory blackbody, the instrument response functions for each of the 152 detectors, at each of the several wavelengths for which they are used, is determined from appropriate Planck functions and diffraction corrections. Before calibrating the airborne spectrum with the laboratory response functions, it is first necessary to correct for telescope transmission and for atmospheric transmission. Both transmissions are measurable functions of wavelength and are characterized by auxiliary measurements. Finally, the product of the measured airborne spectrum and the instrument response function, divided by the atmospheric and telescope transmission functions, yields the actual spectrum of the object.

While it is obviously easier to obtain the ratio of α Boo or Ceres to the spectrum of Sirius or Vega and then to use a theoretical spectrum of one of these hot stars to calibrate the α Boo spectrum, the correctness of the theoretical spectrum must ultimately be verified over the full spectral range in which it is applied. The Kurucz models (see Cohen et al. 1992: Paper I) were constructed to incorporate what is known about the stars and their visible and UV spectra. The models yield spectra extending into the infrared. Using such a model to extrapolate beyond 17 μm is unjustified in the case of Vega because of its circumstellar dust cloud (Aumann et al. 1984). While the Infrared Astronomical Satellite (IRAS) did not reveal a cloud around Sirius, it could not have recognized a departure from model predictions if that departure was common to all stars. Consequently, it is important to bring closure to the measurement of celestial standards by comparing spectra calibrated against theoretical models to spectra calibrated against laboratory standards. Such closure might have been obtained by using asteroid spectra as absolute standards provided that models of sufficient accuracy were available. While existing models incorporate effects of size, phase, surface texture and distances from Sun and Earth, they do not include the effects of mineral composition on spectra (Cohen et al. 1998: Paper VIII). In any case, this

paper offers spectra of both α Boo and Ceres calibrated against a laboratory blackbody and compares them with our previous results which ultimately are based on our calibrated spectral model of Sirius (Paper I) as the primary standard.

Section 2 offers a brief review of how the raw celestial spectra were obtained. In Section 3 the laboratory calibration approach is described. This depends upon diffraction corrections. These are detailed in Appendix A. Section 4 presents the results of the laboratory calibrations, followed by a discussion (Section 5) of differences between spectra obtained by laboratory standards compared to those based on model atmospheric spectra. Section 6 briefly focuses on the surface mineralogy of Ceres.

2. α Boo and Ceres

The spectra of celestial objects were obtained using the High-efficiency Infrared Faint-Object Grating Spectrometer (HIFOGS) at the Nasmyth focus of the KAO. HIFOGS contains 120 Si:Bi detectors for the 3 μm to 18 μm spectral range and 32 Si:Sb detectors for 15 μm to 30 μm. It is a liquid-helium-cooled, grating spectrometer described elsewhere (Witteborn et al. 1995). HIFOGS was used with a 1.5 mm entrance aperture (20″ field-of-view) with a resolving power ranging from 100 to 200 across each spectral band chosen. The spectrometer provides a choice of two gratings, remotely selectable, as well as remotely selectable bandpass filters, so two spectral bands could be observed in a given flight. Additional choices of wavelength coverage were made by external control of the grating angle. The spectral ranges covered during each flight are shown in Table 1.

3. Laboratory calibration approach

The objective of this research is to calibrate the spectral flux of two celestial sources against a well-understood laboratory source of radiation. The major elements of the calibration including blackbody source, transfer optics, modulation, diffraction effects and transmission corrections are discussed in this section.

The reference source used in this work is a UK National Physical Laboratory (NPL) blackbody whose design ensures the Planckian nature of emitted radiation (Chu et al. 1994). The cavity is a cylinder, 70 mm in diameter and 400 mm long, with a 20 mm exit aperture. The output flux is constant to 1 K across 16 mm of this 20 mm aperture and decreases by no more than 20 K at the edge of the aperture when the blackbody is at its maximum temperature of 423 K. The inside of the cavity is coated with oxidized stainless steel but relies on multiple reflections to ensure emissivity of 0.999 or better from 0.9 μm to 30 μm. The radiance temperature of the cavity was determined using contact probes calibrated traceable to the ITS-90. The equivalence of the temperature as determined from the contact probes compared to the radiance temperature has been demonstrated by comparison to the primary standard blackbody at the NPL, verifying this performance (Chu et al. 1994). Almost all the external length of the cavity is surrounded by circulating oil to ensure uniform temperature of the cavity walls. Two accurately calibrated platinum resistance thermometers monitor the uniformity of the oil bath which reaches $\leq$4 mK (limited by our measurement uncertainty in the difference between the two probes) after about two hours at a given temperature setting. One probe can be placed in any of 6 different locations within the oil bath while the other penetrates both oil bath and the outer wall of the cylindrical cavity. When the differences between the cavity probe's reading and that in any of these locations in the oil are $\leq$4 mK we begin to make measurements. Temperature regulation to the 4 mK level can be maintained at any chosen temperature

between 50° C and 140° C. The total estimated 2σ uncertainty in effective radiance temperature is ± 0.13 K (r.m.s. average), resulting from the combined effects of standard source calibration, alignment errors, readout digitization and reproducibility.

Optics for transferring radiation from the NPL source to the spectrometer were mounted in the transfer optics chamber (TOC) shown in Figure 1. The purpose of the TOC is to image the pinhole source aperture (nominal diameters from 100 μm to 270 μm) onto the spectrometer entrance aperture with the same f/ratio and obscuration provided in the KAO. To achieve this, we included a mask on the first TOC mirror encountered by radiation leaving the NPL cavity that represents a correctly scaled central circular obscuration and four scaled spider legs. Thus contributions to diffraction and obscuration experienced by light traveling from the telescope entrance to the spectrometer entrance are duplicated in the TOC. The chamber and the space between the NPL blackbody and the entrance aperture are purged with dry nitrogen to prevent spectral absorption by water and CO_2. The NPL blackbody radiation is modulated by a harmonic chopper placed close to the source aperture. The "limiting" aperture (1.778 mm radius) is located between the chopper and the NPL source and sized to constrain all lines-of-sight from the pinhole source aperture to cross through the blackbody exit aperture or else strike the blackened wall surrounding the limiting aperture. This wall, the chopper, the pinhole source aperture wall and the entire TOC, including its optical surfaces, are all well connected thermally so that they are effectively at the same temperature. An insulated aluminum box surrounds the airtight TOC so that dry ice can surround the optical path from the limiting aperture up to 3 cm from the spectrometer entrance. Eight of the spectrometer's detectors are monitored to record DC levels. All are monitored for AC. The DC level is sensitive to total incident flux, which is usually dominated by foreground radiation. These levels are used to verify that the foreground conditions in the TOC (cooled by dry ice) were similar to those in the KAO at 12.4 km. The interface between the TOC and the spectrometer is airtight. The

purge gas is injected near the spectrometer and has the length of the chamber to equilibrate with the cold chamber walls. Purge gas is also injected into a plastic bag enclosing most of the NPL blackbody. This gas provides an over-pressure between the NPL blackbody exit region and the insulated limiting aperture near the chopper.

The spectral shape of the modulated radiation reaching the spectrometer from the NPL source is the difference between the source Planck function and the radiation from the chopper, multiplied by a diffraction correction. The diffraction correction is dominated by effects of the source aperture and the limiting aperture. When the geometry is well known the diffraction effects may be calculated accurately. Calculations specific to the TOC geometry are described in Appendix A. A check on the realism of the geometrical description, as well as the overall method, was made by measuring spectra from the NPL source using three different source aperture diameters and comparing the ratios of spectra from any two source apertures with the calculated ratios. As seen in Figure 2, the ratio of spectra through a 202 μm diameter hole to that through a 262 μm hole agrees quite well with the shape of the calculated ratio from 3 μm to 30 μm. The 6% vertical displacement is probably caused by a small difference in beam alignment between the two measurements, as inferred from the value of the ratio extrapolated to very short wavelength. The ratio of spectra through a 104 μm aperture to that through a 202 μm aperture is in agreement from 3 μm to 10 μm. At longer wavelengths, significant differences arise, possibly related to the finite aperture thickness (40 μm). Consequently, only measurements made with the 202 μm aperture are used for calibration in this paper.

Since the chopper emissivity $\epsilon(\lambda)$ is not as well known as that of the NPL blackbody, the detector response function, $R(\lambda)$, was initially determined by measuring the spectral outputs from the NPL blackbody at two different temperatures, T_1 and T_2. Let the measured detector signals corresponding to T_j be $S(j, \lambda_i)$ for each detector i. (i ranges

from 1 to 152.) The subscript i will be dropped from λ in all subsequent notation. If the chopper temperature T_{ch} is held constant then the radiation entering the spectrometer is $[P(T_j,\lambda) - \epsilon(\lambda)P(T_c,\lambda)]D(\lambda,c)$, where $D(\lambda,c)$ is the diffraction correction calculated in Appendix A using pinhole source radius c and $P(T_j,\lambda)$ is the Planck function for temperature T_j. (We always monitored the chopper temperature during these measurements but found no significant variations.) The detector response function is thus (for each wavelength λ)

$$R(\lambda) = [P(T_2,\lambda) - P(T_1,\lambda)]D(\lambda,c)/[S(2,\lambda) - S(1,\lambda)]. \quad (1)$$

While this approach eliminates the need to know $\epsilon(\lambda)$, the variances in measuring S(2,λ) and S(1,λ) are additive. We can use

$$R(\lambda) = [P(T_j,\lambda) - P(T_c,\lambda)]D(\lambda,c)/S(j,\lambda), \quad (2)$$

provided that we can establish that $\epsilon(\lambda)$ is sufficiently close to unity over the wavelength range. This can be done by comparing the results of Eq. (2) for two widely different temperatures T_j, typically 322 K and 363 K. The results were found to be identical within experimental uncertainty, so that Eq. (2) was usually used. This enables us to apply the unused data set as an independent check.

4. Application of laboratory calibration

The response function, $R(\lambda)$, determined in the previous section may be applied directly to the airborne raw spectra, $W(\lambda)$, once these are corrected for atmospheric transmission, $A(\lambda)$, and telescope transmission, $t(\lambda)$, to yield the true, flux calibrated spectrum, $F(\lambda)$.

$$F(\lambda) = W(\lambda)R(\lambda)/A(\lambda)/t(\lambda) \quad (3)$$

In practice, the spectra are obtained in segments because of limitations of the grating efficiency. Each segment corresponds to a wavelength range indicated in Table 1. The 5 μm

to 9.4 μm segments have considerable overlap with the 8 μm to 14 μm segments. Spectra in the latter segments have a systematic deviation from the former that is largest in the first few channels that are sampled. Inspection of the wave form during sampling of the 160 channels (152 AC outputs + 8 DC outputs) shows a capacitive rise time in response after a chop cycle starts. Although efforts were made to work at precisely the same frequency in the KAO (7 Hz) as in the laboratory, the tuned laboratory chopper worked only at 6.6 Hz when the final laboratory measurements were made. In any case, matching the phasing precisely was not feasible. The overlap region of the spectrum enables us to establish an empirical correction function for the improper phasing in sampling. To remove this phase effect, all $W(\lambda)$ segments were divided by the function 1-exp[-0.020(n_0+n)]), where n is the channel number in order of the time of sampling and n_0 was 108 for flight data taken 1995 May 4, and 61 for flight data taken 1995 April 19. The constants were determined by an empirical match of the overlap in the fluxed α Boo spectra.

Note that, during all our KAO flights devoted to calibration work, we restricted the flow of the helium boil-off in the HIFOGS cryostat to maintain a sea-level (laboratory) atmospheric pressure, to minimize any differences between the operating temperature of the HIFOGS detector arrays on the KAO and in the laboratory.

The atmospheric transmission was calculated using the "ATRAN" software tool (Lord 1992). Altitudes of 11.9 km to 12.5 km were known from the recorded flight profile of the KAO. Precipitable water vapor measurements were available from some flights, but are not as reliable as information from our own spectrometer. The atmospheric transmissions were calculated at several values typically encountered by the KAO at 11.9 km and higher, from 4 to 12 μm of precipitable water in the line-of-sight. The transmission curve that best removed the terrestrial water signature from the star or asteroid spectrum was chosen. This procedure is reasonable because water on the asteroid would be ice, and in the stellar

atmosphere, a very hot vapor. In either case, the absorption profile is much different from that of terrestrial water. Neither Ceres nor α Boo is likely to have sufficient water to affect our measurements. We were not able to match the measured ozone features using the calculated transmissions. Consequently, data from 9.4 μm to 9.8 μm have been deleted.

The telescope transmission was measured by directing a collimated, chopped infrared light source through the KAO optical path and into the spectrometer mounted in its normal observing location at the Nasmyth focus. The cavity was purged with dry nitrogen. The collimated beam was only 10 cm in diameter, so only a small part of the primary was sampled. After sampling all spectral segments, the infrared source was focused directly on the spectrometer entrance, again through a purged optical path. Unfortunately the KAO cavity purge was not adequate to eliminate strong water vapor absorption features, so the reflectivity measurements had to be repeated using individual optical components in the laboratory, where a better purge could be maintained. Even so, the KAO cavity tests did provide the surprising result that there was no SiO absorption feature in the KAO transmission spectrum. This feature was easily measured in an earlier laboratory reflectivity test on an old KAO witness sample which was coated with 770Å of SiO over an aluminum substrate. It produced a 4% absorption feature centered near 8 μm with a FWHM $\sim$ 1 μm. When the back-up tertiary, which had the same coating that was on the primary, was tested for reflectivity, it also failed to exhibit any absorption feature more than 2% deep in the wavelength range 3 μm to 14 μm and more than 4% (the accuracy of the measurement) deep from 15 μm to 30 μm. We conclude either that no protective overcoat was applied to the KAO optics during its most recent aluminization, or that the coating was worn off in subsequent washing. The dichroic beam splitter, which was used in the KAO measurements but not in the laboratory, was found to have flat (near unity) reflectivity from 3 μm to 14 μm with no absorptions exceeding 2% of the average continuum. The absorption was between 0% and 5% in the 15 μm to 20 μm spectral range. In the 20 μm to 25 μm spectral

range, absorption was between 0% and 10%; it was zero, to within 5%, in the 25 μm to 30 μm band.

The telescope spectral transmission (not including gray absorption) is determined by three reflections from aluminum surfaces, characterized by the tertiary, and one by our dichroic beam splitter. To within our measurement uncertainty there was no deviation from flat response to within 2% per surface from 3 μm to 14 μm. From 15 μm to 30 μm, the deviations from flat response did not exceed 4% per surface for the 3 reflections from aluminum surfaces. The dichroic beam splitter varied from 0% to as much as 10% absorption in the 20 μm to 25 μm range, but was otherwise like the aluminum surfaces. The measurement uncertainties were larger from 20 μm to 25 μm, but all reflectivities are consistent with a flat spectral response. Consequently, $t(\lambda)$ was assumed to be unity at all wavelengths.

The fluxed spectrum of α Boo resulting from Eq. (3) is compared in Fig. 3 to the spectrum determined using Vega as a primary standard (3 μm to 14 μm) and using IRAS Low Resolution Spectrometer (LRS) data and an Engelke (1992) function to extrapolate to 30 μm (Paper VII). They are plotted as the product $\lambda^4 F_\lambda$ versus λ to facilitate the comparison. We plot Ceres data fluxed with Eq. (3) in Fig. 4, showing a theoretical Standard Thermal Model (STM) with beaming factor of unity (cf. Paper VIII) for comparison.

5. Discussion of differences from standards based on models

In Fig. 3a, the α Boo spectrum determined from laboratory standards rises as much as 15% above the Engelke function used to extrapolate values based on the IRAS LRS data in our published α Boo spectrum (Paper VII). Several data points near 12 μm and 25 μm

fall more than 3σ above the trend of the rest of the data. These points are associated with detectors that are especially sensitive to alignment error (between the spectrometer and the TOC). These points are retained in the averaging and statistical uncertainty calculations used in Fig. 3b. In Fig. 3b, a 5-point boxcar average is plotted from 3 μm to 14 μm and the entire spectral band in a given grating setting is averaged for data at wavelengths greater than 15 μm. The long-wavelength uncertainty bars are the standard deviations of the mean of all points in the band. Within these uncertainties there is no significant deviation of laboratory calibrated flux from that based on the Engelke function past 15 μm. This puts a constraint on a thin, warm dust ring or other unexpected contributions to the thermal infrared not already ruled out by IRAS 60 μm and 100 μm photometry. It is worth noting that the uncertainty resulting from reflectivity measurements of the telescope mirrors in the 15 μm to 20 μm and the 25 μm to 30 μm bands is in only one direction: deviation from the assumed unit transmission could raise the long wavelength fluxes a maximum of 15% above those shown in Fig. 3. The box-car averaging masks an apparent spectral feature near 16 μm as discussed below.

The laboratory-calibrated spectrum falls below the published standard near 3 μm and again near 4 μm. The 3 μm to 4 μm spectra were taken in second order and thus required both a cut-on filter at 2.9 μm and a cut-off filter at 5.9 μm. The cut-on filter blocked 3rd order radiation and appeared to do so successfully. The cut-off at 5.5 μm was a sapphire filter which permitted some leakage from longer wavelengths to appear in the 3 μm to 4 μm spectrum. Since the cool laboratory blackbody spectrum rises steeply with increasing wavelength while the star spectrum decreases, a significant error can result from long-wavelength leakage. We recalibrated at higher blackbody temperatures and found closer agreement with the archive-calibrated data, as would be expected if the leakage radiation became a smaller fraction of the total in the laboratory spectrum. We could not completely eliminate the effects of leakage and, consequently, adopt our published

"composite" spectrum (Paper VII) as the reliable standard in the 3 μm to 5 μm range.

In Fig. 4, the laboratory-calibrated Ceres spectrum agrees in shape with the model from 5 μm to 14 μm. Differences may be attributed to mineral absorption features as discussed in Paper VIII. The data beyond 15 μm suggest a cooler component to the Ceres emission but, as discussed below, we are more confident of the broadband accuracy of the spectrum when calibrating using the archive α Boo standard (Paper VII).

In Fig. 4 we note a few isolated deviant points with small uncertainties. As noted for Fig. 3a, we do not think that these are real features in the spectra. but rather the effects of boresight or alignment mismatch between airborne and laboratory spectra. A few of the detectors are more sensitive to this problem. The purpose of the Fabry optics, placed just ahead of the detectors in the optical path (see Witteborn et al. 1995), is to minimize this effect, but laboratory tests in which the focused beam is moved across the spectrometer aperture reproduce the effect.

In Fig. 5, the Ceres spectrum is calibrated against α Boo and fluxed using our Paper VII α Boo reference spectrum. The results past 15 μm have not previously been published and offer an alternative standard to stellar sources provided thermal models are used to scale the spectrum to other heliocentric and geocentric distances, and phase angles. We consider the observations in Fig. 5 to be a more accurate spectrum in overall shape than the measurements presented in Fig. 4, because of systematic uncertainties that arise in matching boresight (optical path) between telescope and laboratory spectra. However, within any band (see Table 1), the small scale features in Fig. 4 are more precise than those in Fig. 5 beyond 20 μm, because Ceres is so much brighter than α Boo and statistical uncertainties for the latter become large at these wavelengths. We note that there is a broad dip in both Figs. 3a and 4 at 16 μm that is absent in Fig. 5. Such a feature could be caused by absorption on a telescope surface or in the atmosphere. We did not find such

a feature when we measured reflectivities of the various surfaces and it does not appear in the calculated atmospheric transmission. We do not think that it is a real feature in either α Boo or Ceres. It could conceivably be a volatile condensate associated with the telescope flight environment.

In summary, we estimate the total uncertainty in the spectra presented. The uncertainty in the α Boo spectral irradiance, Fig. 3b, arises from the statistical spread shown in the figure (ranging from 2% at 6 μm to 25% at 28 μm) added in quadrature to the systematic uncertainties. The latter are dominated by telescope transmission uncertainty. The transmission is the product of 3 aluminum mirror reflections and a dichroic beam splitter reflection, all discussed above. These products lie between 1.00 and 0.92 from 3 μm to 14 μm, between 1.00 and 0.84 from 15 μm to 20 μm, between 1.00 and 0.80 from 20 μm to 25 μm, and between 1.00 and 0.84 from 25 μm to 30 μm, resulting in fractional transmission uncertainties of +0/−0.08, +0/−0.16, +0/−0.20. +0/−0.16, respectively. The contributions to flux uncertainty have the reverse sign. The remaining quantifiable systematic uncertainties are approximately $\pm$0.02 for atmospheric transmission (outside of the strong bands), $\pm$0.02 for errors in flux arising from blackbody alignment and chopper surface characterization, $\pm$0.02 for effects of aperture/geometry uncertainty on diffraction corrections. There were additional uncertainties from small differences in alignment and radiation foreground of the KAO environment and that produced in the laboratory. Comparison of data from 3 different flights and numerous laboratory tests shows that these affected the entire spectrum by the same factor at wavelengths of 6 μm and longer, except for a few detectors which were more sensitive to such effects, as noted earlier in this section. Since we are determining only the shape of the spectrum, the factor does not enter into the uncertainty determination. Adding the statistical and systematic uncertainties in quadrature yields: from 6 μm to 9.4 μm: +9%/−4%; from 10 μm to 14 μm: +11%/−7%; from 16 μm to 20 μm: +21%/−14%; from 20 μm to 25 μm: +24%/−13%;

from 25 μm to 30 μm: +30%/-25%. The total uncertainty in the spectral data for Ceres in Fig. 5 is dominated by the statistical uncertainty (1σ uncertainty bars) assuming that we accept the archive α Boo spectrum as an accurate standard. The uncertainties in the archive standard add only 2% to 3% (beyond 16 μm) to the statistical uncertainties. The systematic uncertainties that contributed to Fig. 3 and 4 are eliminated because both standard and source are viewed through the same telescope, with the same alignment and boresight, nearly the same airmass and identical diffraction losses. This is, of course, the reason that we have labored so hard to establish accurate, widely accessible celestial standards.

6. Implications for Ceres surface mineralogy

From either Fig. 5 or Fig. 4 it is apparent that Ceres has a broad emission plateau from 16 μm or 17 μm to 22 μm or 23 μm, with relatively lower emissivity from 23 μm to 30 μm. In Fig. 6 of Paper VIII, where the 5 μm to 14 μm of Ceres is plotted as an emittance spectrum, we see a sharp rise in emissivity from 8.3 μm to 9.4 μm, a broad plateau from 9.4 μm to 11.4 μm, decreasing to a broad shallow minimum near 13 μm. The behavior of the Ceres spectrum thus follows approximately that calculated for olivine particles by Mukai & Koike (1990) using the Comet Halley dust size distribution (their Fig. 3) and is also similar to their olivine emission coefficient spectrum for 3 μm particles. From 5 μm to 8 μm, olivine exhibits low emissivity, but a mixture with other material could account for the higher emissivity of Ceres at wavelengths below 7.6 μm. The Ceres spectrum from 5 μm to 14 μm is discussed in Paper VIII which relates the 8.3 μm to 11.4 μm behavior to the Christiansen frequency and finds it consistent with silicates having a lower degree of polymerization (e.g., olivine; Salisbury 1993; Kahle et al. 1993). The presence of metal-free olivines has long been expected on asteroid surfaces as a result of debris ejection from differentiated

asteroids (Bell et al. 1989; Burbine 1994). Much of the search has been confined to the near-infrared where reflection spectra offer diagnostic olivine features seen in several small asteroids (e.g., Cloutis et al. 1993). These features are not observed in Ceres. As noted in Paper VIII, however, Ceres is large enough to retain very fine-grained dust, whereas small asteroids are depleted in small dust grains (Dollfus 1989). Such dust may form a thin layer of micron-sized particles on the surface of Ceres as the result of the collection of pulverized chondritic material collisionally ejected from other asteroids or other parts of Ceres. Le Bertre and Zellner (1980), for example, conclude that Vesta's surface has particles larger than 50 μm coated with particles smaller than 10 μm. While much more information is needed, the data presented here suggest that the olivine-rich asteroids may be found using longer wavelengths that can penetrate the thin overlying, fine-dust layer.

7. Conclusions

The use of laboratory flux standards to calibrate celestial sources presents serious challenges in reducing systematic uncertainties. In these measurements the long wavelength region (15 μm to 30 μm) proved to be most difficult because of measurement uncertainties in the telescope transmission. Overall, the 3 μm to 5 μm and the 6 μm to 30 μm portions of the laboratory-calibrated spectra agree to within 2 standard deviations of the published α Boo based models for hot stars. The wavelength-degraded, laboratory-calibrated spectrum, Fig. 3b, is within 1 standard deviation of the models beyond 6 μm. The agreement between the α Boo spectra calibrated against a laboratory blackbody and our previously published α Boo spectrum, calibrated ultimately against a theoretical model, confirms the assumptions implicit in the models. For normal stars, limits on the order of 25% may be placed on any infrared excess above model predictions. The Ceres spectrum based on stellar standard spectra appears to be an adequate secondary standard from 5 μm to 30 μm. It

differs significantly from models which, so far, do not account for mineralogical features or large-scale variation in topography. The similarity of the 8 μm to 30 μm Ceres spectrum to calculated olivine emissivity spectra suggests further study to determine whether this silicate is indeed widespread on Ceres.

We thank the crew and staff of the Kuiper Airborne Observatory (now retired from service) for their generous and enthusiastic support. We are also indebted to D. Scimeca and D. Lesberg for fabrication of the laboratory calibration chamber and the reflectometer, to A. Meyer and D. Scimeca for assistance in laboratory calibrations, to S. Sandford and M. Bernstein (Astrochemistry Group) for auxiliary reflectivity measurements (3 μm to 20 μm) and to J. Farhoomand and C. Koeber for auxiliary reflectivity measurements (14 μm to 30 μm). We thank the Cornell Astronomy Dept. and Rockwell, Inc. for permission to use the Si:Sb 1×64 array that they developed under a NASA/SIRTF grant. It is a pleasure to thank Dr. Graham Machin of the UK National Physical Laboratory both for his initial advice and recommendations on the particular style of reference source to commission from NPL, and for undertaking the characterization, validation, and accreditation of our NPL cavity. MC thanks NASA-Ames for support through Co-operative Agreement NCC 2-142 with Berkeley. FCW thanks NASA-Ames for support through Co-operative Agreement NCC2-900.

A. Appendix

For the wavelengths considered, corrections for diffraction losses are needed to accurately relate source spectral radiance and detector response in the laboratory blackbody flux measurements. Only after such corrections are applied is the geometrical throughput of an experimental configuration effectively realized. Two of the configurations tested featured pinhole source apertures with radius c=101 μm or 131 μm, located between a ρ=1.778 mm radius limiting aperture (fully illuminated by the blackbody), and the r=6.35 mm radius pupil (Fig. 6). The 1.778 mm aperture and pupil were 150 mm apart, and the pinhole was a=23 mm from the former and b=127 mm from the latter. To assess the largest losses, it is adequate to consider throughput of the combination, 1.778 mm aperture + pinhole + pupil. However, additional losses also occurred because of a 100 mm separation between the 1.778 mm aperture and the 20 mm diameter blackbody opening. Despite the large dimensions of both of these, proximity of the blackbody opening perimeter to the pinhole's field of view exacerbated the effect of diffraction losses resulting from the 1.778 mm aperture.

To assess the latter losses as well as the former, it was necessary to simulate the propagation of radiation through the blackbody opening, 1.778 mm aperture and pinhole aperture in series. In doing this, radiation incident on each optic was computed based on the radiation incident everywhere on the preceding optic, including all accumulated diffraction effects. (The above losses are not additive, nor are their effects on throughput multiplicative.) We have used Kirchhoff's scalar diffraction theory, so that the radiation field on each aperture is given by

$$\psi(\mathbf{r}'') = (i\lambda)^{-1} \int_{\text{preced. ap.}} d^2\mathbf{r}' \, [\exp(2\pi i|\mathbf{r}'' - \mathbf{r}'|/\lambda)/|\mathbf{r} - \mathbf{r}'|] \, \psi(\mathbf{r}'),$$

where $\mathbf{r}''$ is the vector normal from the axis to a location on the aperture and $\mathbf{r}'$ is a vector normal from the axis to any location within the preceding aperture. In the above expression, the Kirchhoff integral assumes (correctly) that the normal derivative of ψ on an

aperture can be approximated as $2\pi i\psi/\lambda$. An ideal, isotropic spectrum of plane waves was assumed to be incident on the blackbody opening.

To insure reliability of the calculations we have computed losses with and without taking into account the 100 mm separation between blackbody and 1.778 mm aperture. Results which neglect the separation are readily confirmed by simpler calculations done within the Fresnel or Fraunhofer approximations. Losses obtained with and without such a separation are presented for sample wavelengths in Table 2. Diffraction effects are succinctly expressed, at each wavelength λ, as the unitless ratio, F_1, of the actual throughput to the geometrical throughput. Deviation of F_1 from unity indicates the diffraction loss. Clearly, the greatest source of loss is because of the pinhole, but a relative loss as large as 6% of F_1 is also incurred because of the separation.

The simpler Fresnel or Fraunhofer calculations can be done as follows. In the present case (*viz.*, $ar < b\rho$), F_1 is most easily expressed in terms of three unitless parameters:

$$u = (2\pi/\lambda)c^2(1/a + 1/b),$$

$$v = (2\pi/\lambda)c\rho/a,$$

$$\sigma = (r/b)/(\rho/a).$$

In particular, the present case also meets the criterion, $u < v(1-\sigma)$. Thus, because the rays are sufficiently paraxial, one has (Shirley 1998),

$$F_1 \approx 2v^2/(\pi u^2\sigma^2) \cdot \int_0^\sigma d\sigma'\sigma' \int_0^1 d\zeta\zeta \int_0^{2\pi} d\theta \left|\alpha(u, v\sqrt{\sigma'^2 + \zeta^2 - 2\zeta\sigma'\cos\theta})\right|^2, \qquad \text{(A1)}$$

where $\sigma'/\sigma = \mathbf{r}''/r$ and $\zeta = \mathbf{r}'/\rho$. The angle θ is the relative azimuthal polar angle between $\mathbf{r}'$ and $\mathbf{r}''$. In this context, $\mathbf{r}'$ and $\mathbf{r}''$ are on the 1.778 mm aperture and pupil, respectively. Within the Fresnel approximation, which is applicable here, one has, for arbitrary u and w,

$$|\alpha(u,w)|^2 = U_1^2(u,w) + U_2^2(u,w).$$

Lommel U functions are given by

$$U_n(u,w) = \sum_{s=0}^{\infty} (-)^s (u/w)^{n-2s} J_{n+2s}(w),$$

where J's denote Bessel functions. One often considers $u \ll w$, and even the Fraunhofer approximation, $|\alpha_{\rm Fraun}(u,w)|^2 = (uJ_1(w)/w)^2$ can prove sufficient.

Equation (4) can be made more convenient by rewriting it as two equations, each of which contains a single integration. Defining (for arbitrary u and w)

$$K(u,w) = \int_0^w dw' w' |\alpha(u,w')|^2,$$

one may derive (Shirley 1998)

$$F_1(u,v,\sigma) = [2/(\pi u^2)] \int_{-1}^{1} dx \sqrt{(1-x^2)[(2+\sigma x)^2 - \sigma^2]} \cdot K(u, v(1-\sigma x))/(1+\sigma x). \quad \text{(A2)}$$

Accounting for finite σ treats the extended nature of the source aperture properly. The substitution, $\sigma \to 0$ in Eq. (5), would neglect displacements of diffraction patterns' centers from the optical axis for effective point emitters arranged throughout the source aperture. Under such a substitution, one would find $F_1(u,v,0) = 1 - J_0^2(v) - J_1^2(v) + ...$, where keeping only the terms shown gives the familiar Fraunhofer result. Accounting for finite σ removes unphysical oscillations of F_1 with λ. This happens because the diffraction rings (for most point emitters) are not centered on the pupil. For a typical emitter, portions of both dark and bright rings in the diffraction pattern lie on the entrance's perimeter.

F_1 for both pinholes is shown in the Table 3 for sample wavelengths. Results were obtained using Fraunhofer and Fresnel approximations for $|\alpha(u,w)|^2$ and using our full Kirchhoff treatment of diffraction effects but neglecting the blackbody-source aperture separation. The agreement supports validity of that treatment. Finally, further calculations which also incorporated optics within the spectrometer supported the separability of laboratory diffraction losses and effects of those optics.

Table 1: Journal of observations

Date	Time UT	Object	Grating gr/mm	Order	Spectral range (μm)
1995 April 19	04:45–05:21	Ceres	90	1st	4.90–9.40
		Ceres	90	1st	4.52–9.4
1995 April 19	05:24–06:00	Ceres	20	1st	15.96–20.44
		Ceres	20	1st	15.71–18.0
		Ceres	20	1st	20.44–25.0
		Ceres	20	1st	25.0–30.0
1995 April 19	07:17–07:30	α Boo	90	1st	4.90–9.40
		α Boo	90	1st	4.52–9.4
1995 April 19	07:35–09:20	α Boo	20	1st	15.96–20.44
		α Boo	20	1st	15.71–18.0
		α Boo	20	1st	20.44–25.0
		α Boo	20	1st	25.0–30.0
1995 May 4	03:44–04:10	Ceres	75	1st	7.92–14.0
		Ceres	75	1st	8.36–14.0
1995 May 4	06:15–06:27	α Boo	90	1st	4.90–9.40
1995 May 4	06:29–06:59	α Boo	90	2nd	3.0–4.1
1995 May 4	07:05–07:52	α Boo	75	1st	7.92–14.0
		α Boo	75	1st	8.36–14.0

Table 2: Sample values of F_1 for several values of λ which ignore (separation = 0 mm) and respect (separation = 100 mm) the blackbody-source aperture separation ("sep.").

λ (μm)	F_1, c = 101 μm		F_1, c = 131 μm	
	sep. = 0 mm	sep. = 100 mm	sep. = 0 mm	sep. = 100 mm
10	0.841	0.836	0.879	0.859
15	0.740	0.728	0.811	0.786
20	0.635	0.617	0.731	0.702
25	0.528	0.506	0.650	0.617
30	0.431	0.409	0.566	0.532

Table 3: Sample values of F_1 for several values of λ for both pinholes, as given by three methods of calculation for the 1.778 mm aperture + pinhole + pupil combination.

λ (μm)	F_1, $c = 101$ μm			F_1, $c = 131$ μm		
	Fraunhofer	Fresnel	Full	Fraunhofer	Fresnel	Full
5	0.920	0.921		0.939	0.938	
10	0.842	0.842	0.841	0.880	0.878	0.879
15	0.741	0.741	0.740	0.812	0.811	0.811
20	0.636	0.636	0.635	0.732	0.731	0.731
25	0.529	0.530	0.528	0.651	0.651	0.650
30	0.433	0.434	0.431	0.568	0.568	0.566

REFERENCES

Aumann H.H. et al. 1984, ApJ, 278, L23

Bell, J. F., Davis, D.R., Hartmann, W.K., & Gaffey, M.J. 1989, in Asteroids II, 921-945

Burbine, T. H., 1994, Meteoritics, 29, 453.

Cloutis, E. A. 1993, 24th Lunar and Plan. Sci. Conf. Part 1, A-F, 317.

Chu, B., McEvoy, H.C. & Andrews, J.W. 1994, Meas. Sci. Technol., Vol 5, pg12

Cohen, M., Walker, R. G., Barlow, M. J. & Deacon, J. R. 1992, AJ, 104, 1650 (Paper I)

Cohen, M., Witteborn, F.C., Carbon, D.F., Davies, J.K., Wooden, D.H., & Bregman, J.D. 1996, AJ, 112, 2274-2285 (Paper VII)

Cohen, M., Witteborn, F. C., Roush, T., Bregman, J., & Wooden, D. H. 1998, AJ, 115, 1671 (Paper VIII)

Engelke, C. W. 1992, AJ, 104, 1248

Kahle, A. B., Palluconi, F. D., & Christiansen, P. R. 1993, in Remote Geochemical Analysis, ed. C. M. Pieters & P.A.J. Englert (Cambridge: Cambridge Univ. Press), 99.

Lord, S. D. 1992, A New Software Tool for Computing the Earth's Atmospheric Transmission of Near-Infrared and Far-Infrared Radiation, NASA TM-103957.

Mukai, T. & Koike, C. 1990, Icarus, 87,180.

Salisbury, J. W. 1993, in Remote Geochemical Analysis, ed. C. M. Pieters & P.A.J. Englert (Cambridge: Cambridge Univ. Press), 79.

Shirley, E. L. 1998, in press (Applied Optics)

Witteborn, F. C., Cohen, M., Bregman, J. D., Heere, K. R., Greene, T. P. & Wooden, D. H. 1995, in Airborne Astronomy Symposium on the Galactic Ecosystem, ASP Conference Series, Vol 73, eds: M. R. Haas, J. A. Davidson & E. F. Erickson, 573-578

This manuscript was prepared with the AAS LaTeX macros v4.0.

B. Figure Captions

Fig. 1.— Laboratory calibration facility. The NPL blackbody provides a stable, well-calibrated source of radiation which is then modulated and optically transferred to the HIFOGS spectrometer through a chamber that simulates the KAO optics and temperature.

Fig. 2.— Ratio of flux from a 202 μm diameter hole to that from a 262 μm diameter hole: measured (top) and calculated (lower - see Appendix A). Difficulty in precisely centering radiation from the larger hole in the spectrometer aperture is the most likely cause of the vertical displacement of the data from the calculated curve.

Fig. 3.— a) α Boo spectrum, $\lambda^4 F_\lambda$, calibrated using a laboratory blackbody, compared to the archive (Paper VII) spectrum based on our calibrated Kurucz model of Vega (Paper I). Uncertainty bars denote 1σ statistical uncertainties only. b) Same as (a), but the 3 μm to 14 μm range has been smoothed with a 5-point boxcar average and the 15 μm to 30 μm range has been degraded spectrally to 4 photometry points representing averages over each of the 4 separate measurements required to cover it: 15 μm to 18 μm (Si:Bi), 15.9 μm to 20 μm (Si:Sb), 20.4 μm to 25 μm (Si:Sb) and 25 μm to 30 μm (Si:Sb). Bars denote the standard deviation of the mean of the values in the bands.

Fig. 4.— The spectrum of Ceres calibrated using a laboratory blackbody, compared to a STM with unit beaming factor, computed for the date and time of observations. Bars denote 1σ statistical uncertainties only.

Fig. 5.— The spectrum of Ceres calibrated using the archive α Boo spectrum and compared with the same STM as in Fig. 4 (Cohen et al. 1992).

Fig. 6.— Displayed from left to right (unfolded, not to scale) are the blackbody opening (radius=10 mm), the ρ=1.778 mm radius aperture (that limits the portion of the blackbody seen at the pinhole source), the pinhole source itself (greatly exaggerated, radius c), and the pupil (radius r). Distances between these optics, the optical axis, and extremal rays are indicated.

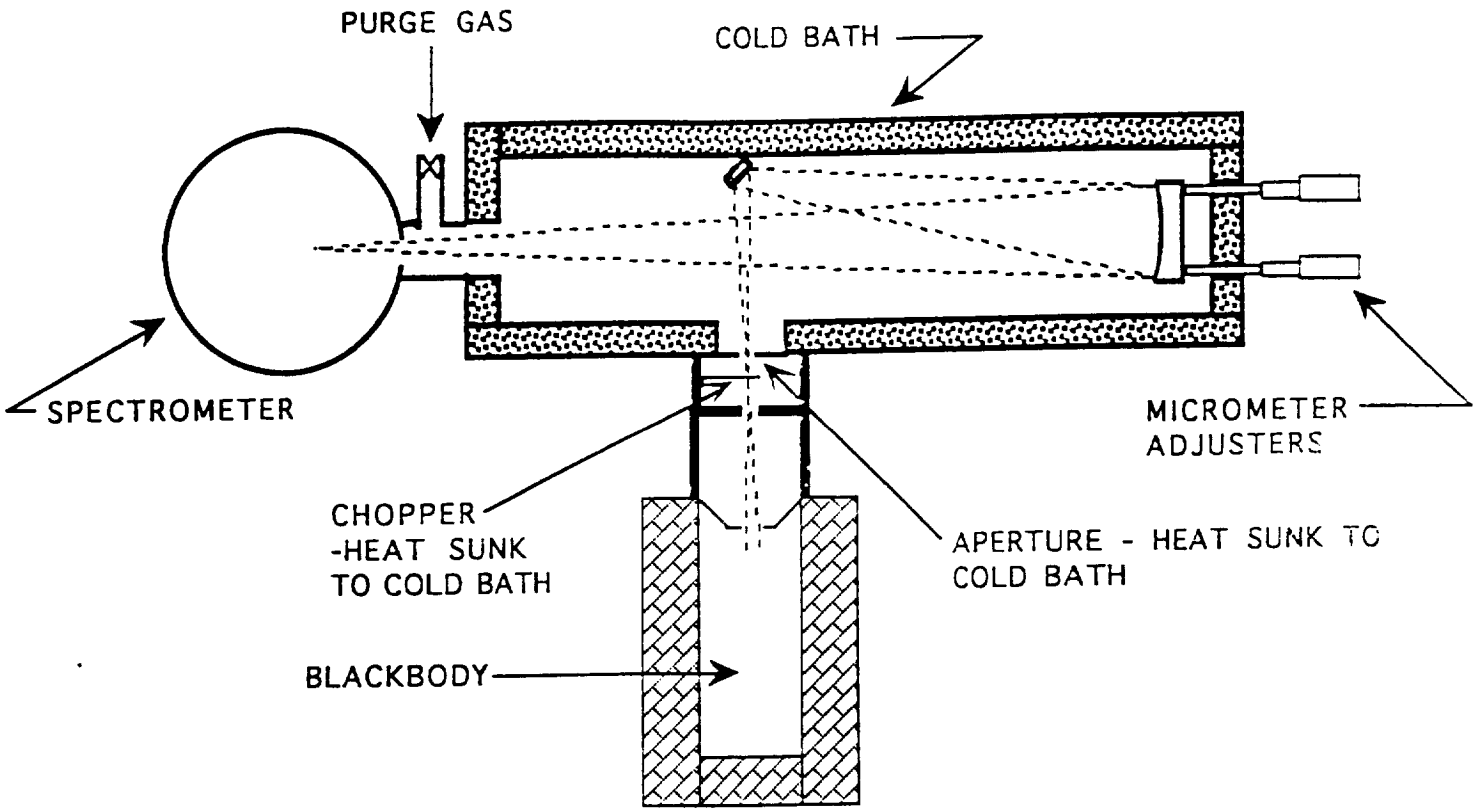
PURGE GAS
COLD BATH
SPECTROMETER
MICROMETER
ADJUSTERS
CHOPPER
-HEAT SUNK
TO COLD BATH
APERTURE - HEAT SUNK TO
COLD BATH
BLACKBODY

Fig. 1

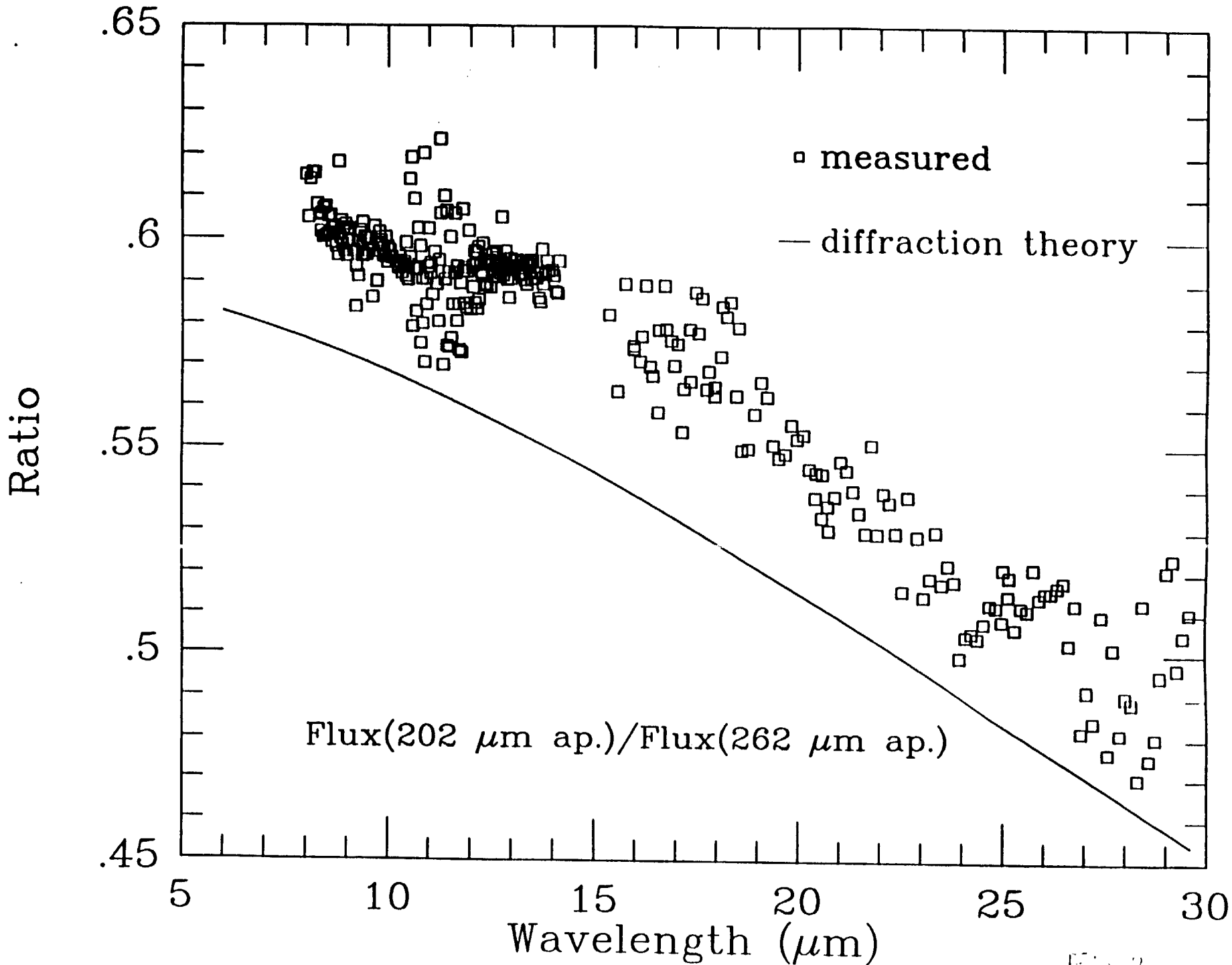
.65
.6
.55
.5
.45
Ratio
5
10
15
20
25
30
Wavelength (μm)
measured
diffraction theory
Flux(202 μm ap.)/Flux(262 μm ap.)

Fig. 2

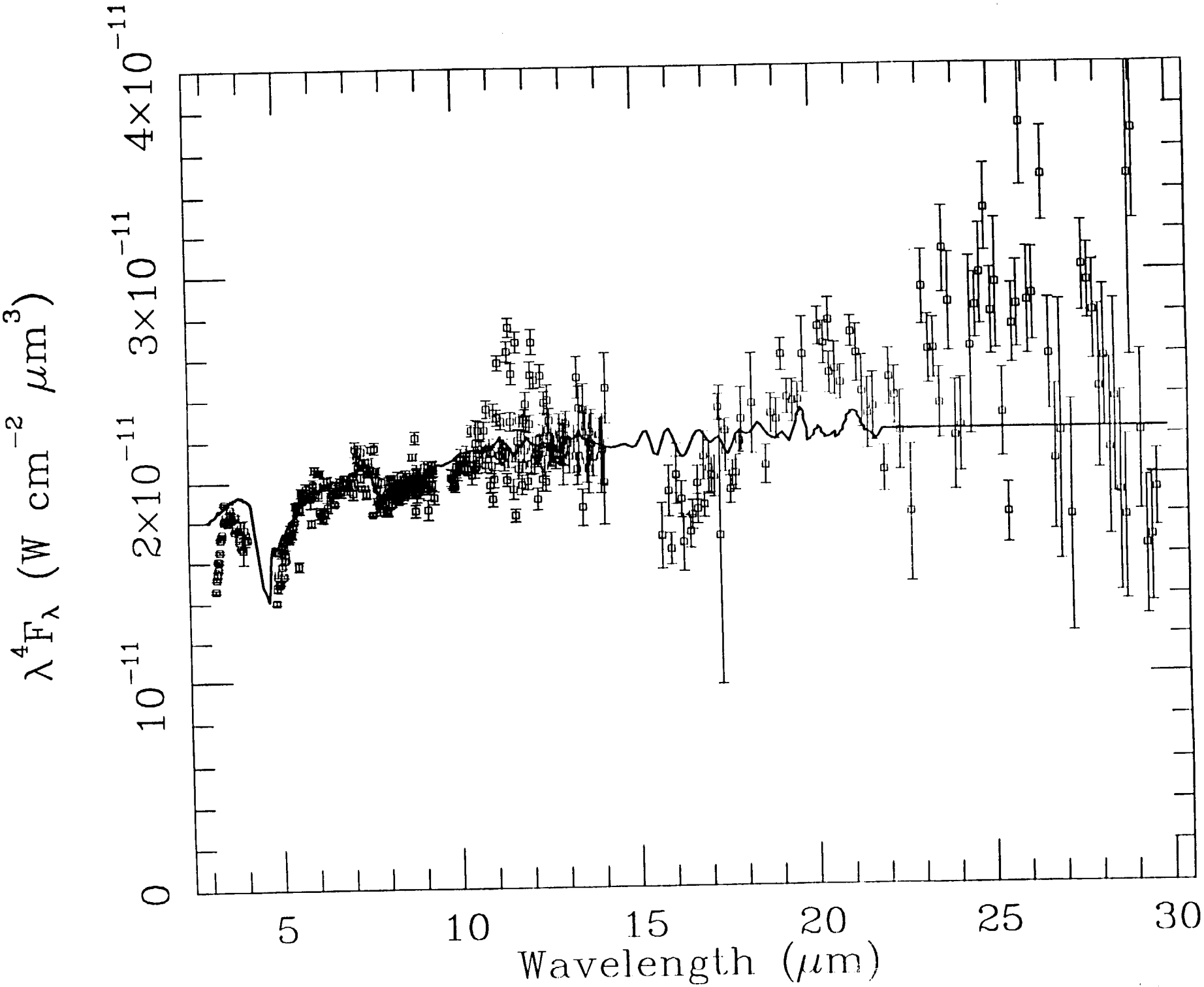
$\lambda^4 F_\lambda$ (W cm^{-2} μm^3)
0
10^{-11}
2×10^{-11}
3×10^{-11}
4×10^{-11}
5
10
15
20
25
30
Wavelength (μm)

$\lambda^4 F_\lambda$ (W cm^{-2} μm^3)
0
10^{-11}
2×10^{-11}
3×10^{-11}
4×10^{-11}
5
10
15
20
25
30
Wavelength (μm)

F_λ (W cm^{-2} μm^{-1})
0
5×10^{-16}
10^{-15}
1.5×10^{-15}
5
10
15
20
25
30
Wavelength (μm)

F_λ (W cm^{-2} μm^{-1})
0
5×10^{-16}
10^{-15}
1.5×10^{-15}
5
10
15
20
25
30
Wavelength (μm)

Fig. 6, Paper XI